1    **INFLUENZA A VIRUS RIBONUCLEOPROTEINS FORM LIQUID ORGANELLES AT**

2    **ENDOPLASMIC RETICULUM EXIT SITES**

3

4    Marta Alenquer[1], Sílvia Vale-Costa[1], Ana Laura Sousa[1,2,§],Temitope Akhigbe Etibor[1,§], Filipe

5    Ferreira[1] and Maria João Amorim[1,*]

6

7    [1] Cell Biology of Viral Infection Lab, Instituto Gulbenkian de Ciência, Oeiras, Portugal

8    [2] Electron Microscopy Facility, Instituto Gulbenkian de Ciência, Oeiras, Portugal

9

10    [§] Equal contribution

11    *Corresponding author

12

13    Tel:          + 351 214407905

14    Fax:          + 351 214407970

15    Email        mjamorim@igc.gulbenkian.pt

16

17

1

18    **ABSTRACT**

19    Influenza A virus has an eight-partite RNA genome that during viral assembly forms a

20    supramolecular complex containing one copy of each RNA. Genome assembly is a selective

21    process driven by RNA-RNA interactions and is thought to lead to discrete punctate structures

22    scattered through the cytosol. Here, we show that contrary to the accepted view, formation of

23    these structures is not dependent on RNA-RNA interactions among distinct viral

24    ribonucleoproteins (vRNPs), as they assemble in cells expressing only one vRNP type. We

25    demonstrate that these viral inclusions display characteristics of liquid organelles, segregating

26    from the cytosol without a delimiting membrane, dynamically exchanging material, deforming

27    easily and adapting fast to hypotonic shock. We provide evidence that they develop close to the

28    Endoplasmic Reticulum Exit Sites (ERES), being dependent on continuous ER-Golgi vesicular

29    cycling. We show that viral inclusions do not promote escape to interferon response, and

30    propose that they facilitate selected RNA-RNA interactions in a liquid environment of

31    concentrated vRNPs.

32

33

34

35      **MAIN TEXT**

36      Influenza A infections are serious threats to human health causing annual epidemics and

37      occasional pandemics[1]. The virus contains an eight-partite RNA genome, and each segment is

38      encapsidated as an individual viral ribonucleoprotein (vRNP) complex. vRNPs are composed of

39      single-stranded negative-sense RNA, with base paired terminal sequences originating a double

40      stranded RNA portion where the trimeric RNA-dependent RNA polymerase (RdRp), composed

41      of PB1, PB2 and PA, binds. The remaining sequence attaches several copies of unevenly-

42      bound nucleoprotein (NP)[2]. The advantages of having a segmented genome are evident for

43      viral evolution[3] and for better gene expression control[4], but increase the complexity of the

44      assembly of fully infectious virions[5-8].

45      Viral assembly occurs at the plasma membrane and, in 80% of the cases, 8 distinct

46      vRNPs are packaged selectively into a budding membrane[9]. Seminal work established the

47      requirement of cis-acting and intersegment RNA-RNA interactions for the formation of this

48      supra-molecular complex (reviewed in[5-8]). However, it is under debate if vRNPs reach the

49      plasma membrane already as complete genome bundles.

50      Upon exiting the nucleus, where they replicate, vRNPs accumulate around the

51      microtubule organizing centre[10] and, subsequently, distribute throughout the cytoplasm

52      concentrating in discrete puncta that enlarge as infection progresses[10-14]. Each puncta

53      accommodates different vRNP segments with the diversity in vRNPs increasing proportionally to

54      the proximity of the plasma membrane[11,13]. Such observation led to the proposal that genome

55      assembly preceded vRNP packaging in budding virions by a process intimately linked with the

56      formation of the referred vRNP hotspots[6,11,13-15]. Studies on the biogenesis of vRNP hotspots

57      showed that their formation requires the cellular GTPase Rab11[10,12,16,17]. In uninfected cells,

58      Rab11 is the master regulator of the endocytic recycling compartment (ERC), one of the

59      systems the cell uses for delivering endocytosed material, as well as specific cargo from the

60      *trans-Golgi-Network* (TGN), to the cell surface[18]. The process is very well-described for

3

61    uninfected cells, with Rab11-GTP regulating ERC transport by recruiting molecular motors,

62    tethers and SNARES to respectively drive, dock and fuse vesicles to the plasma membrane[18].

63    Despite initial reports that the functional role of Rab11 was to deliver vRNPs to the cell

64    surface[10,12,17,19], accumulating evidence analyzing Rab11 sub-cellular localization and non-

65    abundancy in virions[14,16,20], binding partners[14] and host transferrin recycling[14,21] strongly

66    indicates that Rab11 is redirected and its function is impaired during IAV infection. In fact, it was

67    demonstrated that vRNPs outcompeted Rab11 effectors for Rab11 binding, rendering the

68    recycling process sub-optimal[14]. Further corroborating the scenario that Rab11 pathway is

69    impaired with infection, a recent publication showed that Rab11 was re-routed to the ER during

70    IAV infection[16]. In addition, using correlative light and electron microscopy, vRNP hotspots were

71    shown to concentrate clustered vesicles positive for Rab11, surrounded by electron dense

72    material[14].

73         The formation of vRNP hotspots was postulated to be dependent on the establishment

74    of sequential RNA-RNA interactions occurring as Rab11 vesicles transporting vRNPs

75    collided[6,11,13,22,23]. However, the impaired ERC hypothesis above mentioned, argues against the

76    requirement for RNA-RNA interactions in the formation of vRNP hotspots and challenges the

77    IAV assembly model proposed. Nevertheless, the existence of vRNP/Rab11 hotspots indicates

78    segregation from the cytosol in foci that are not delimited by membranes, although they

79    contain numerous remodeled membranes inside[14,15]. Sub-organelles not delimited by

80    membranes are abundant in the viral world and are known as viroplasms, viral factories,

81    aggresomes or virosomes, to indicate sites of viral replication[24-26]. Viruses can also form viral

82    inclusions and these are sites of accumulation of viral proteins, nucleic acid and selected host

83    proteins and can include viral factories or not[24,25]. Given this definition, IAV vRNP hotspots could

84    be re-classified as viral inclusions. The most notable cases of electron dense aggregated

85    material in the cytosol (not delimited by membranes) are found in cells infected by viruses of

86    DNA (*Poxviridae, Iridoviridae, Asfaviridae*), of dsRNA (*Reoviridae*) and of negative-sense RNA

87    genome (*Paramyxoviridae, Rhabdoviridae, Filoviridae*)[24-29]. Formation of factories is associated

88    with remodeling of host membranes and/or cytoskeleton to orchestrate sophisticated platforms

89    for viral replication and/or for escaping host immune recognition[26]. However, several questions

90    remain unclear relative to the internal organization and biophysical properties of these cellular

91    condensates. Resolving these questions for IAV will help to understand the rules and physical

92    properties of organizing cellular matter into membraneless organelles in the virus world and

93    identify their functions.

94         In this manuscript, we show that vRNP/Rab11 hotspots constitute viral inclusions that

95    are not delimited by membranes and display characteristics of liquid organelles. Liquid

96    properties include dynamic change of components, round appearance, easy deformation upon

97    application of sheer force or fusion events and fast adaptation to physiological changes. We

98    show that the liquid organelles are formed in the vicinity of the Endoplasmic Reticulum Exit Sites

99    (ERES) (or transitional ER) and their assembly is dependent on continuous ER-Golgi vesicular

100   cycling. We demonstrate that, contrary to the current view, these sites are not formed by

101   established RNA-RNA interactions amongst different vRNP segments, but precede viral

102   genome assembly. We propose that the condensed IAV inclusions do not promote escape to

103   the antiviral response but facilitate stochastic RNA-RNA interactions in a liquid environment of

104   crowded vRNPs.

105

106

107   **Results**

108       **vRNPs and Rab11 form rounded viral inclusions that are not membrane delimited.**

109       Using electron microscopy, we previously showed that viral infection induced clustering

110   of vesicles heterogeneous in size[14]. These constitute, in high percentage, round-shaped

111   molecular concentrates, enriched in membranes at the core, but interestingly not delimitated

112   from the cytosol by membranes (Fig. 1a, yellow arrows and quantification in Supplementary Fig.

113   1). Such structures are found in cells infected by many viruses and known as viral inclusions, as

114   they concentrate viral (and cellular) material[24,25]. In agreement, using correlative light and

115   electron microscopy, areas of clustered vesicles/viral inclusions matched those of vRNPs and

116   Rab11 identified by immunofluorescence[14]. Using double immunogold labelling, we confirmed

117   the existence of electron dense regions (green arrowheads) positive for vRNPs, protruding from

118   vesicles (red arrowheads) positive for Rab11 (Fig. 1b). To investigate whether the lack of

119   membrane enabled viral inclusions to react fast to physiological changes or whether they

120   constituted crystallized aggregated material, we subjected them to hypotonic shock. Infected

121   cells expressing GFP-NP to label vRNPs[30] were live-imaged by confocal microscopy. After

122   approximately 1 min, cells were subjected to a rapid hypotonic shock (the ionic strength

123   changed from 150 to 0.300 mM by diluting media with water). Viral inclusions, otherwise stable

124   over time, immediately started to dissolve, and 2 min later were no longer visible (Fig. 1c,

125   Supplementary Movies 1 and 2). The ability of the IAV viral inclusions to react to dilution

126   suggests a liquid character[31]. Together, these data reveal that viral inclusions, containing both

127   Rab11 and vRNPs, can respond to changes in the cellular environment and their constituents

128   can self-organize into fluxional spherical structures in live cells, behaving like a membraneless
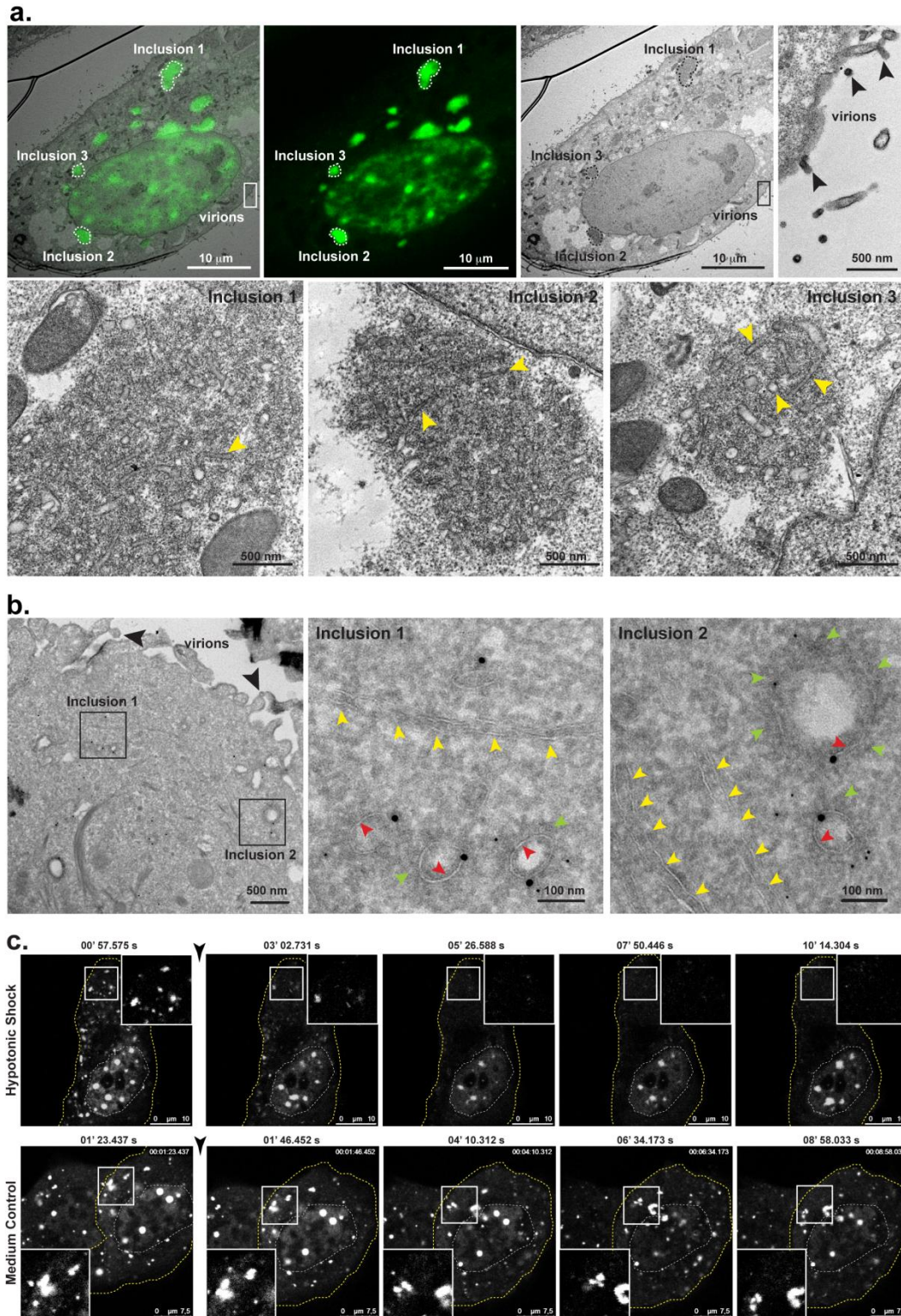
129   organelle.

130

131

**Figure 1. vRNPs and Rab11 form membraneless organelles that quickly respond to changes in the cellular environment**

134   **a.** HeLa cells were transfected with a plasmid encoding GFP-NP and co-infected with PR8 virus, at an MOI of 10.

135   Cells were imaged by confocal and electron microscopy and the resultant images were superimposed. Areas of

136   correlation, inclusions 1 to 3, are delineated by a dashed line in the upper panel and shown in greater detail in the

137   lower panel. Progeny virions budding at the surface (black arrowheads) show that the cell was infected. Yellow

138   arrowheads show individual vesicles within the inclusion. Bar = 10 $\mu$m or 500 nm. **b.** GFP-Rab11 WT cells were

139   infected with PR8 virus, at an MOI of 5, for 16 h. Cells were stained for GFP (18 nm gold particles) and viral NP (6 nm

140   gold particles). Inclusion areas are highlighted by black boxes. Yellow arrowheads indicate ER structures in the

141   vicinity of viral inclusions. Black arrowheads show progeny virions budding at the cell surface. Red arrowheads show

142   Rab11 vesicles. Green arrowheads show electron-dense vRNPs. Bar = 100 or 500 nm. **c.** A549 cells were

143   transfected with a plasmid encoding GFP-NP and co-infected with PR8 virus, at an MOI of 5. At 16 hpi, cells were

144   imaged under time-lapse conditions. The black arrowhead indicates addition of water (hypotonic shock) or regular

145   growth medium. White boxes highlight vesicular clusters in the cytoplasm in the individual frames. The dashed white

146   line marks the cell nucleus, whereas the dashed yellow line delineates the cell periphery. Bar = 7.5 or 10 $\mu$m. Images

147   were extracted from Supplementary Movies 1 and 2. Experiments were performed at least twice.

148

149   **vRNPs form viral inclusions with properties of liquid organelles.**

150   Many membraneless organelles have been described in the cell, being supramolecular

151   assemblies formed by nucleic acids and proteins[32]. Examples include nuclear speckles,

152   nucleolus, centrioles and stress granules[33,34]. Interestingly, these were shown to have liquid-like

153   properties on account of their dynamic exchange of material, ability to internally reorganize,

154   rounded shape, and deformability promoted by fusion and fission events[32,35]. Recently, Negri

155   bodies formed during rabies virus infection were shown to have liquid-like properties[27], and it

156   was postulated that other viral factories or viral inclusions among *Mononegavirales* would

157   assemble by liquid-liquid phase separation. To test this idea for influenza A viral inclusions, we

158   analysed their dynamic nature inside living cells. We observed that viral inclusions were highly

159   dynamic, as demonstrated in Fig. 2a (and Supplementary Movie 3). To capture the movement

160   of a 1 min movie in a snapshot, we show the average intensity of labelled vRNPs (in red) as a

161   defined puncta, surrounded by a wider green area that corresponds to the standard deviation of

162    the average, indicating that these structures are highly dynamic (Supplementary Movie 3). We

163    then enquired if individual clusters exchanged material with the exterior and performed

164    fluorescence recovery after photobleaching (FRAP). We found a high variation in the behavior

165    of cytosolic viral inclusions, with different speeds and patterns of recovery of the fluorescent

166    signal. Some exhibited a fast and complete recovery (Fig. 2b, purple line, Supplementary Movie

167    3), whilst others showed a slower and incomplete recovery (Fig. 2b, blue line, Supplementary

168    Movie 3). The recovery profile was also variable with some regions losing and/or gaining

169    intensity during the recovery phase (Fig. 2b, purple line) but others exhibiting a steady

170    progression of fluorescence recovery (Fig. 2b, blue line). Not surprisingly, when the collection of

171    FRAP events was averaged, the recovery profile obtained had a very large standard deviation

172    (Fig. 2c). The calculated half time of recovery was 2.9 seconds and the diffusion rate calculated

173    was $2.422 \pm 0.154$ m$^{-13}$ s$^{-1}$ (D $\pm$ SEM), a value similar to what has been found for other liquid

174    organelles including Negri bodies formed during rabies virus infection[27].These measurements

175    are also consistent with those of nucleoli and stress granules[27,36], indicating that viral inclusions

176    exchange material with similar structures or with the cytosol. The mobile fraction of vRNPs

177    varied from $41.4 \pm 15.7\%$ (mean $\pm$ SD) at 5 seconds to $63.5 \pm 39.7\%$ within 60 seconds, and the

178    curve plateaued after 15 seconds (Fig. 2c). The immobile GFP-NP must be biologically relevant.

179    It either translates thermodynamically stabilized or kinetically trapped state of the protein, as in

180    stable interactions (presumably among different vRNPs in each cluster), or a complex pattern of

181    exchange between vRNPs and the exterior. In fact, careful analysis of dynamic events of

182    individual viral inclusions revealed a constant flux of small material in and out of these rounded

183    structures (Fig. 2d, arrows, Supplementary Movie 4), many fusion events amongst individual

184    inclusions either separated at short or long distance (Fig. 2e, Supplementary Movies 5 and 6)

185    and fission events (Fig 2f, Supplementary Movie 6). Upon fusion/fission events, the rounded

186    shape was reacquired, indicating occurrence of internal rearrangements. Some acquisition of

187    material originated from several compartments being difficult to track their origin (Fig. 2e,

9

188    complex, Supplementary Movie 6). Collectively, these data suggest that vRNP/Rab11 inclusions

189    are liquid droplets arising from phase separation. Furthermore, these inclusions appear to be

190    constantly exchanging material amongst them, which would be essential if these were sites

191    devoted to viral genome assembly.



192
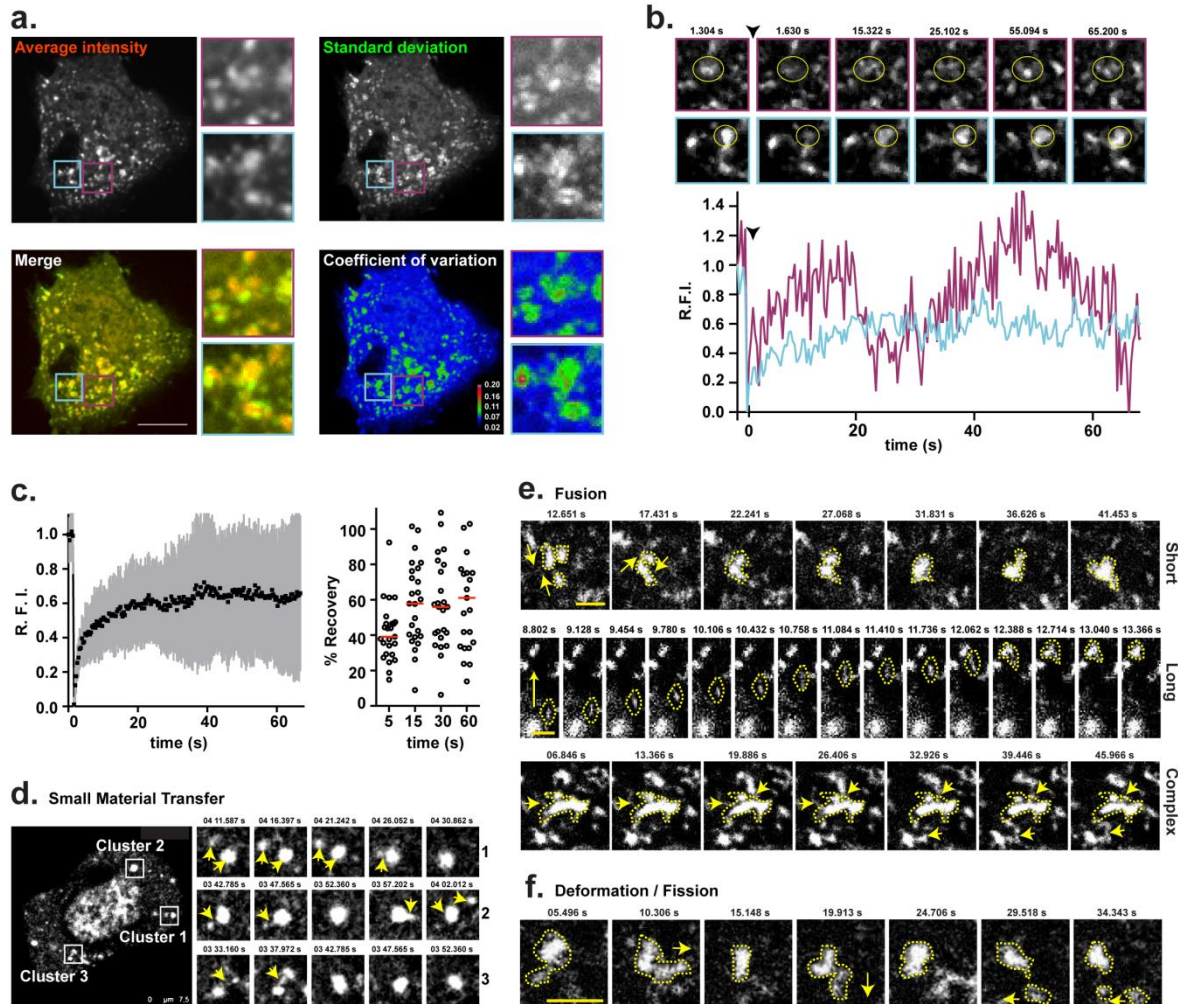
**Figure 2. vRNP/Rab11 inclusions have properties of liquid organelles and exchange material dynamically**

A549 cells were transfected with a plasmid encoding GFP-NP and co-infected with PR8 virus, at an MOI of 5, for 16

h. Cells were imaged under time-lapse conditions. **a.** A representative infected cell is shown. The fluorescence signal

of viral clusters in this cell is depicted as: average intensity (in red), standard deviation (in green), the merge of both,

and coefficient of variation. Two areas of viral NP inclusions, highlighted in purple and cyan boxes, were selected for

fluorescence recovery after photobleaching (FRAP). Bar = 10 μm **b.** The photobleached regions are marked by a

yellow circle. The black arrowhead indicates the time of photobleaching. Relative fluorescence intensity (R.F.I.) was

200    plotted as a function of time for each particle. Images have been extracted from Supplementary Movie 3. **c.** R.F.I.

201    was plotted as a function of time for the means of 25 FRAP events (left graph). The means are shown (black) with

202    error bars representing the standard deviation (gray). The percentage of recovery of each photobleached region is

203    shown for specific times (right graph), with means represented as red bars. A single experiment representative of two

204    independent experiments is **d.** A representative infected cell is shown in the large image, with selected clusters

205    marked by white boxes. Individual frames with single moving particles, from each cluster, highlighted with yellow

206    arrows are shown in the small panels. Bar = 7.5 μm. Images were extracted from Supplementary Movie 4. **e.**

207    Individual frames show three distinct fusion events: at short distance – simple and complex – and at long distance. **f.**

208    Similarly, deformation and/or fission event is shown. Yellow arrows highlight fusion (**e.**) or fission (**f.**) movements,

209    whereas yellow dashed lines indicate the shape of clusters. Images were extracted from Supplementary Movies 5

210    and 6. Bar = 2 μm.

211

212    **IAV viral inclusions form when a single vRNP is expressed in cells.**

213    The most accepted model establishes that RNA-RNA interactions lead to the formation

214    of viral inclusions. However, the dynamic exchange of material within clusters supports that

215    these structures promote genome assembly. The formation of viral inclusions, measured by

216    redistribution of Rab11, was reported on a mini-replicon system expressing only two vRNPs,

217    segment 7 and 8[10], for which no particularly strong RNA-RNA interactions have been

218    demonstrated[37,38]. In addition, vRNPs self-repulse and compete to avoid repetition of a vRNP in

219    a virion[39-41]. We tested whether RNA-RNA interactions were needed to form the liquid viral

220    inclusions by assessing the formation of vRNP hotspots and the sub-cellular distribution of

221    Rab11 in the same mini-replicon system expressing one or two segments.  Cells were

222    transfected with plasmids expressing the RdRp and NP (3P-NP), NS2 (to ensure nuclear export

223    of vRNPs), segment 7 (that encodes for M1 and M2) and, when indicated, segment 8 (that

224    expresses NS1 and NS2). Segment transcription originates a complete negative sense RNA, to

225    which the RdRp binds, amplifying the system, mimicking viral transcription and replication. As

226    control, the same system without the polymerase PB2 was evaluated (2P-NP).

227     Results show that Rab11 subcellular distribution did not change in any of the 2P-NP

228     conditions, consistently with previous reports[10]. However, in the 3P-NP condition, Rab11

229     redistributed, forming the characteristic enlarged puncta regardless of expressing one or two

230     vRNPs, indicating that one vRNP is sufficient to form viral inclusions (Fig. 3a). The increase in

231     areas of Rab11 puncta was significantly different between the 3P-NP and 2P-NP conditions

232     when quantified and ranked based on their size: small inclusions up to 0.15 $\mu m^2$, intermediate

233     inclusions between 0.15 and 0.30 $\mu m^2$, and large inclusions bigger than 0.30 $\mu m^2$ (Fig. 3b), as

234     before[14]. Consistent with our own work, if vRNPs did not exit the nucleus by not including NS2,

235     Rab11 distribution was similar to the 2P-NP condition (Fig 3b, 3P-NP seg7 without NS2).

236     Similarly, in the case of 3P-NP, and independently of the number of segments expressed,

237     vRNPs were detected in puncta, rather than dispersed, showing that vRNP hotspots are formed

238     without requiring RNA interactions among distinct segments (Fig. 3c, upper panels). In the case

239     of 2P-NP conditions, probes against the vRNA of segments 7 or 8 detected discrete dots in the

240     nucleus (Fig. 3b, lower panels), consistent with pol I transcription and lack of amplification, as

241     described before[10]. The expression of all components of each condition was evaluated by

242     western blotting, except that of NS2, for which no good commercial antibody is available (Fig.

243     3d). Confirming that the system was fully functional, the corresponding proteins of a specific

244     segment were detected only in 3P-NP samples (Fig. 3d).

245     Collectively, the obtained results demonstrate that viral inclusions assemble in the

246     presence of a single vRNP. The data indicates that formation of Rab11 enlarged puncta is

247     dependent of vRNPs reaching the cytosol, but precedes and is not dependent on RNA-RNA

248     interactions.

249
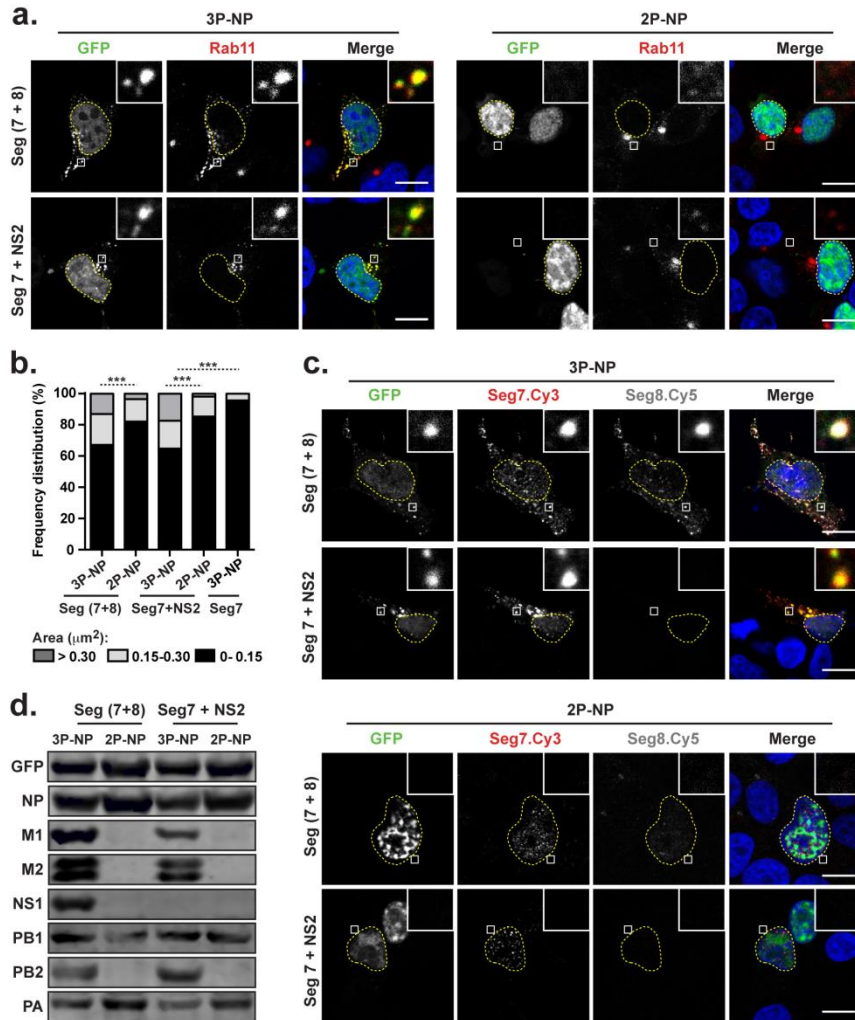
**Figure 3. Viral inclusions form in the absence of RNA-RNA interaction**

293T cells were transfected for 16 h with plasmids expressing vRNA segments 7 and 8, or segment 7 alone, and the minimal protein components of an influenza RNP: the three polymerase proteins (3P) (or, as a nonfunctional control, two polymerase proteins lacking PB2 - 2P) and NP, as well as with plasmids expressing GFP-NP. Cells were also transfected with a plasmid encoding NS2, when segment 7 was expressed alone. **a.** Cells were fixed and stained for Rab11 (red). White boxes show areas of co-localization between NP and Rab11. Nuclei are delineated by yellow dashed lines. Bar = 10 $\mu$m. **b.** The frequency distribution of Rab11 inclusions within the three area categories (in $\mu$m$^2$) was plotted for each condition. Statistical analysis of data was performed using a non-parametric Kruskal–Wallis test, followed by Dunn's multiple comparisons test (***p < 0.001). Statistical analysis compares the area of all inclusions between conditions. Between 30 and 70 cells were analyzed per condition. **c.** Duplicate samples were processed to detect segment 7 (red) and segment 8 (gray) RNA by FISH. White boxes show areas of co-localization

261   between NP and viral segments. Nuclei are delineated by yellow dashed lines. Bar = 10 μm. **d.** Cells were lysed and

262   indicated proteins were detected by Western blotting.

263

264   **vRNP-containing viral inclusions are not responsible for escaping innate**

265   **immunity activation.**

266   It has been shown that phase-separated compartments are able to sequester or exclude

267   specific material, including components of the innate antiviral immune response[42,43]. It is

268   therefore possible that formation of IAV viral inclusions is a strategy to prevent the activation of

269   cell-intrinsic defenses, either by sterically excluding sensors of exogenous material or by

270   sequestering key factors of the downstream pathways. To address this hypothesis, we have

271   used A549 cells constitutively expressing a fully functional or a non-functional form of GFP-

272   tagged Rab11 (GFP-Rab11 wild type (WT) or GFP-Rab11 dominant negative (DN),

273   respectively). These cells were established in our lab, and have been evaluated for growth rate

274   and permissiveness to viral infection[14]. Both cell lines were infected with WT PR8 or an NS1

275   mutant virus that does not express a functional form of the main viral factor supressing cell

276   antiviral responses (NS1-N81)[44]. To characterize viral infection, cells were fixed at 8 and 16 h

277   post-infection (hpi), stained for NP protein and imaged by confocal microscopy (Fig. 4a).

278   Changes in Rab11 subcellular distribution were quantified by measuring the area of Rab11

279   inclusions in infected and control cells, and ranking them as above (Fig. 4b). As previously

280   published by us[14], infection of cells stably expressing GFP-Rab11 WT with WT PR8 virus

281   induced a redistribution of Rab11, forming viral large inclusions that contained vRNPs (Fig. 4b).

282   Furthermore, the frequency of large Rab11 inclusions increased as infection progressed from 8

283   to 16 hpi. Noteworthy, infection of this cell line with the NS1 mutant virus produced similar

284   changes in the frequency distribution of the different size category inclusions (Fig. 4b). Infection

285   of GFP-Rab11 DN cell line, either with WT PR8 or NS1 mutant virus, did not change Rab11 DN

286   distribution (Fig. 4a,b). Consistent with previous reports[12,17,45], Rab11 DN was primarily localized

14

287    to the TGN, with some diffuse cytoplasmic staining also visible (Fig. 4a). Also in agreement with

288    these studies, overexpression of Rab11 DN impaired the formation of viral inclusions

289    characteristic of IAV infection and formation of vRNP hotspots[11,13], and therefore NP was

290    diffusely distributed throughout the cytoplasm (Fig. 4a). Next, we examined the impact of

291    constitutively expressing GFP-Rab11 WT or DN on viral replication, by plaque assay (Fig. 4c).

292    WT PR8 and NS1-N81 virus production in GFP-Rab11 DN cell line was significantly impaired

293    when compared with GFP-Rab11 WT cell line, with an approximately 50% reduction in viral

294    titres at 16 hpi (Fig. 4c). These results corroborate previous studies showing that a fully

295    functional Rab11 protein is required for efficient infectious virus production[12,45]. As expected[46],

296    NS1 mutant virus replication was attenuated in both cell lines, as compared to WT PR8 virus

297    (Fig. 4c). In order to investigate if impaired formation of viral clusters resulted in enhanced

298    activation of the interferon (IFN) cascade, the transcript levels of type I (IFN-$\alpha$ and IFN-$\beta$) and

299    type III (IL-29) IFN, and of the IFN-stimulated gene viperin, were analysed at 8 and 16 hpi. For

300    positive control, cells were transduced with the double-stranded RNA mimic

301    polyinosinic:polycytidylic acid [poly(I:C)]. Results show that there are no differences between

302    both cell lines, in any of the conditions analysed (Fig 4d). Also, NS1 mutant virus induced higher

303    mRNA levels than the WT virus, confirming the IFN-antagonizing role of NS1 (Fig 4d). At the

304    protein level, cell lysates from infected cultures were probed for active, phosphorylated IFN

305    regulatory factor 3 (IRF3), a hallmark of activation of the IFN induction cascade (Fig. 4e), and

306    cell culture media were tested for the levels of secreted IFN-$\beta$ (Fig. 4f). Again, the results

307    obtained were identical for both cell lines. In summary, all results point towards innate immune

308    responses not being affected by biological phase transitions of vRNPs.

309
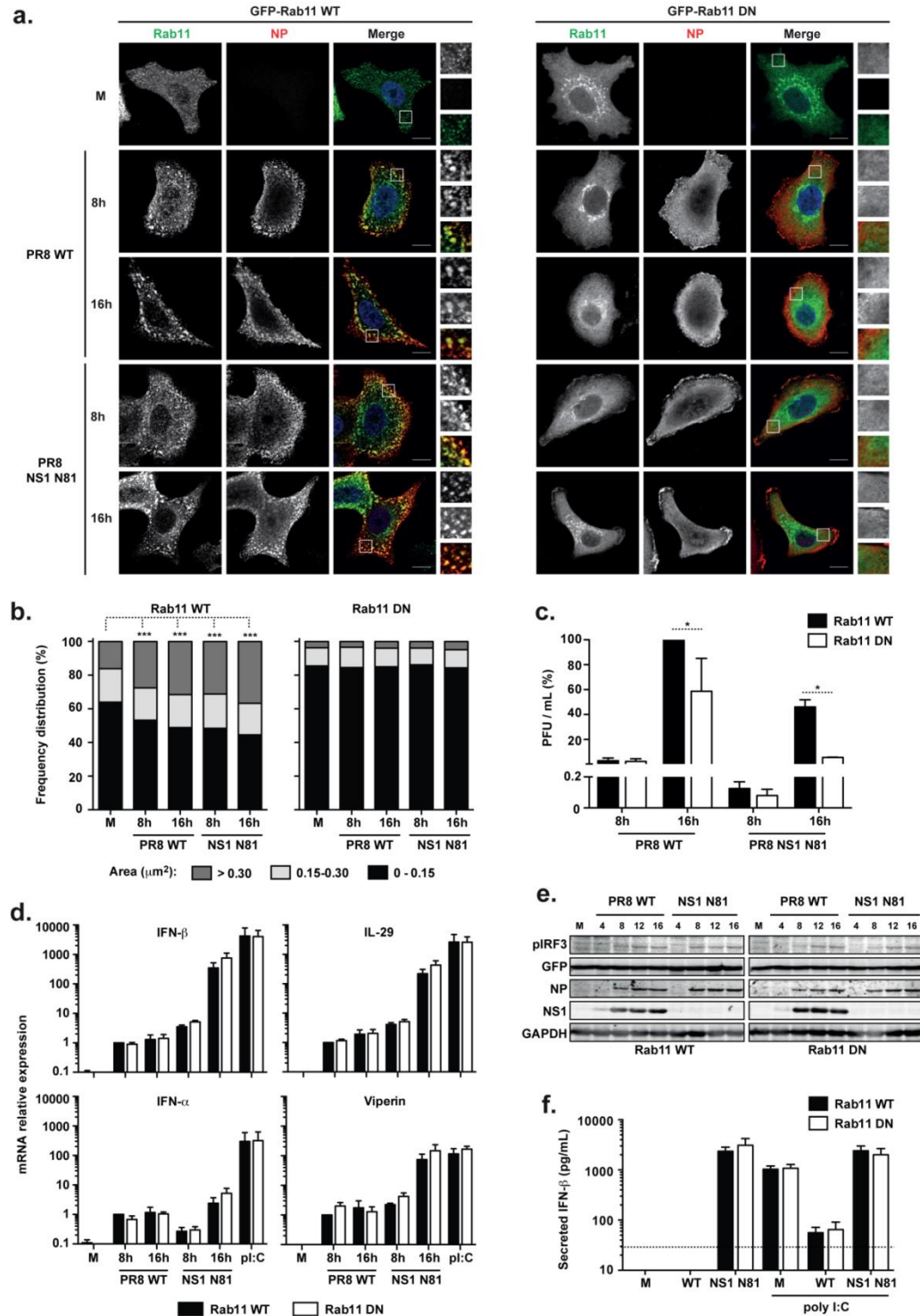
**Figure 4. Cell antiviral defenses are not affected by the formation of viral inclusions**

**a.** GFP-Rab11 WT and GFP-Rab11 DN cells were infected or mock-infected (M), at an MOI of 3, with PR8 WT or NS1-N81 viruses. Cells were fixed at the indicated times and stained for NP (in red). Bar = 10 μm. **b.** The frequency distribution of NP inclusions within the three area categories (in μm$^2$) was plotted for each cell line. Statistical

16

315      analysis of data was performed using a non-parametric Kruskal–Wallis test, followed by Dunn's multiple comparisons

316      test    (*** p < 0.001 for GFP-Rab11 WT cells; no statistical significance found for GFP-Rab11 DN cells). Statistical

317      analysis compares the area of all inclusions between conditions. An average of 30 cells was analyzed per condition.

318      A single experiment representative of two independent experiments is shown. **c.** At the indicated times, supernatants

319      were collected and viral production was evaluated by plaque assays using MDCK cells. Statistical analysis of data

320      was performed using two-way ANOVA test, followed by Sidak multiple comparisons test (*p < 0.05 at 16 hpi; no

321      statistical significance found at 8 hpi). Data represents the average of three independent experiments. **d.** Expression

322      of IFN-$\beta$, IFN-$\alpha$, IL-29 and viperin was evaluated at the level of transcription by RT-qPCR in relation to GAPDH.

323      Poly(I:C) was used as a positive control for maximum expression of these transcripts. Statistical analysis of data was

324      performed using two-way ANOVA test, followed by Sidak multiple comparisons test (no statistical significance

325      between conditions found). Data represents the average of three independent experiments. **e.** Expression of

326      phosphorylated IRF, GFP, NP, NS1 and GAPDH was evaluated at the protein level by western blotting. **f.** The levels

327      of secreted IFN-$\beta$ were quantified by ELISA in cell supernatants at 24 hpi. Poly(I:C) was used as a positive control for

328      maximum expression of IFN-$\beta$ protein. The limit of detection of this method is 30 pg/mL (dashed line). Statistical

329      analysis of data was performed using two-way ANOVA test, followed by Sidak multiple comparisons test (no

330      statistical significance between conditions found). Data represents the average of three independent experiments.

331

332      **Viral inclusions form in the proximity of the ER, displaying matching movements.**

333      Given that phase separation is generally a spatially regulated process, we next asked

334      whether this was the case for IAV viral inclusion assembly. It has recently been reported that

335      vRNPs associate with the ER when leaving the nucleus and that Rab11 would collect vRNPs

336      from the ER for delivery to the surface[16]. Our electron microscopy data also indicates that the

337      ER is constantly found in close proximity to viral inclusions (Fig. 1b, yellow arrowheads). We

338      therefore tested if clusters are associated with the ER, by using antibodies against different ER

339      markers or a cell line expressing a fluorescent tagged-ER membrane marker (HeLa Sec61$\beta$-

340      Emerald)[47].   Confocal imaging of cells at different times post-infection failed to identify co-

341      localization between the ER and viral inclusions (Supplementary Fig. 2a-c). However, it was

342      evident that, from 8 hpi onwards, the vRNP clusters dispersed throughout the cytoplasm were

17

343    frequently found juxtaposed to ER tubules (Supplementary Fig 2a-c, inlets), suggesting an

344    association between both structures. To gain insight into the dynamics of ER-viral inclusion

345    association, live cell imaging was performed. For this, HeLa Sec61β-Emerald cells were

346    transfected with mCherry-NP and infected with PR8 (Fig. 5a and Supplementary Movie 7), or

347    A549 cells were co-transfected with mCherry-NP and ER-GFP and infected with PR8 virus (Fig.

348    5b and Supplementary Movie 8). In both experiments, viral inclusions displayed movements that

349    matched those of the ER, although it is not clear whether ER motion was driving displacement

350    of viral inclusions or, conversely, viral inclusions were gliding over the surface of the ER tubules.

351    The ER is a complex organelle, with distinct morphologies and diverse functions[47-49]. In order to

352    identify the specific ER domain interacting with viral inclusions, we tested different markers,

353    including Atlastin 3, which accumulates in 3-way junctions, Sec23 and Sec31, both present in

354    ER Exit Sites (ERES).  We observed no correlation between Atlastin 3 and vRNPs staining

355    (Supplementary Fig. 2d), but Sec23 and Sec31 localized between the clusters and the ER, and

356    even co-localized with NP in specific spots (Fig. 5c, Supplementary Fig. 2e). Live cell imaging of

357    Sec16, another ERES component, indicates that these structures serve as docking platforms

358    where vRNPs accumulate, allowing a constant flux of material in and out of viral inclusions, with

359    frequent fission and fusion events taking place (Fig. 5d, Supplementary Movies 9 and 10).

360
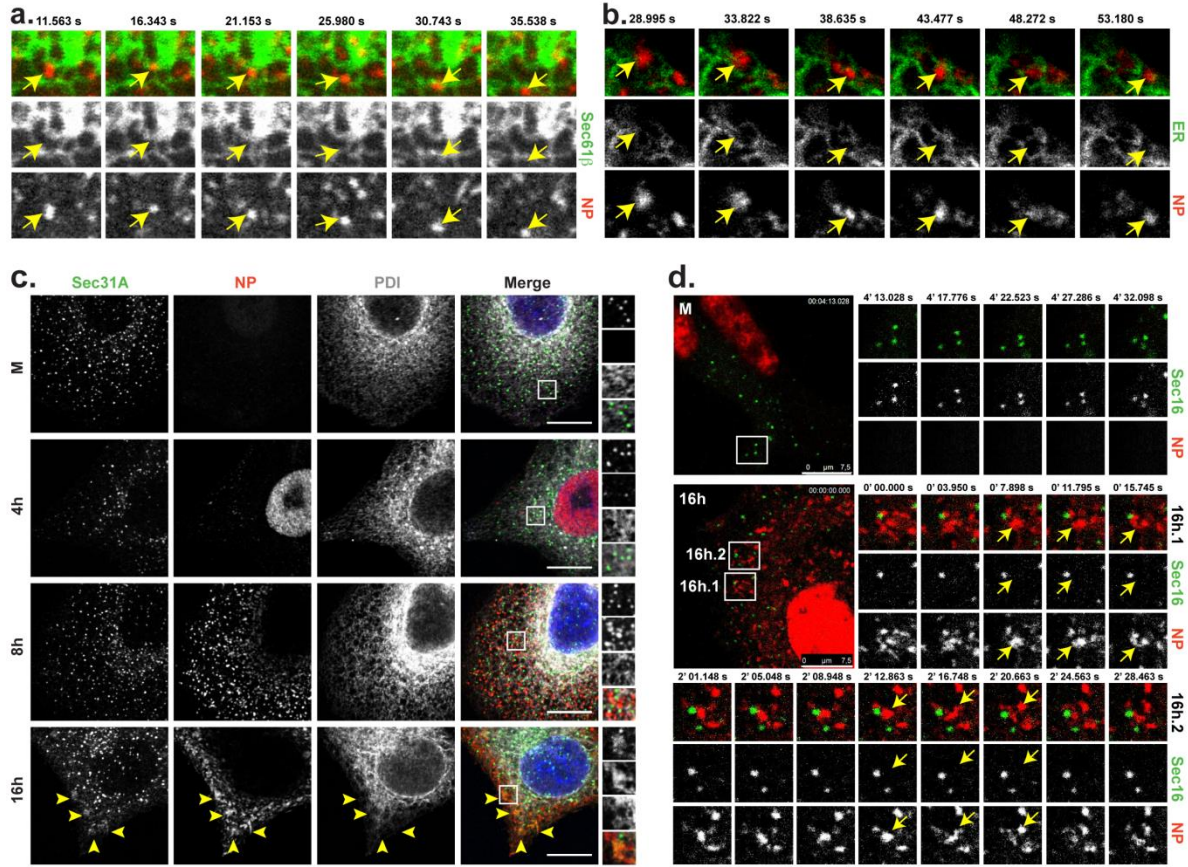
**Figure 5. Viral inclusions are associated with ER exit sites**

**a.** Sec61β-Emerald cells were transfected with mCherry-NP and infected with PR8 virus, at an MOI of 10, for 16 h. **b.** A549 cells were co-transfected with plasmids encoding mCherry-NP and ER-GFP and infected with PR8 virus, at MOI of 10, for 16h. **a., b.** Cells were imaged under time-lapse conditions. Individual frames with single moving particles highlighted with yellow arrows are shown in the small panels. Bar = 2.5 μm. Images were extracted from Supplementary Movies 7 and 8. **c.** A549 cells were infected or mock-infected (M) with PR8 virus, at an MOI of 3, and fixed at the indicated times. Cells were stained for the ER proteins Sec31 (in green) and PDI (in gray) and the viral NP protein (in red). Areas highlighted by the white box are shown on the right of each panel. Bar = 10 μm. **d.** A549 cells were co-transfected with plasmids encoding mCherry-NP and GFP-Sec16 and infected or mock-infected (M) with PR8 virus for 16 h. Cells were imaged under time-lapse conditions. Representative cells are shown in the left large images. Individual frames with single moving particles highlighted with yellow arrows are shown in the small panels. Two examples are provided for the infected cell (16h.1 and 16h.2). Bar = 7.5 μm. Images were extracted from Supplementary Movies 9 and 10.

374

375      **Continuous Golgi-ER vesicular cycling controls the formation of viral inclusions.**

376      The ERES are specialized domains where secretory proteins are loaded into coat

377      protein complex II (COPII)-coated vesicles and transported to the Golgi[50]. Recruitment of COPII

378      proteins to the ERES is controlled by the Sar1 GTPase cycle[51]. This small-GTPase also

379      regulates ER-membrane tubulation and vesicle fission, having a critical role in the generation of

380      the ERES[52]. To analyse the effect of disrupting the ERES on the assembly of viral inclusions,

381      we overexpressed a GTP-restricted mutant of GFP-tagged Sar1 (Sar1-GTP), which inhibits

382      anterograde protein transport. Overexpression of GFP and GFP-tagged Sar1 WT were

383      performed as controls. Immunofluorescence analysis showed that overexpression of Sar1-GTP

384      strongly reduced the size of viral inclusions, when compared to overexpression of GFP or Sar1,

385      in a statistically significant manner (Fig. 6a, b). The number of inclusions per $\mu m^2$ of cellular

386      area and the percentage of NP signal that is inside viral inclusions were also analyzed, with the

387      latter being  significantly reduced when Sar1-GTP was overexpressed [7.7 ± 2.9% (mean ± SD)

388      in Sar1-GTP vs 12.7 ± 3.8% in GFP (p<0.0001) and 11.1 ± 3.4% in SAR1 (p=0.0005)] (Fig. 6b).

389      Confocal imaging of the viral transmembrane protein hemaglutinin (HA) confirmed that Sar1-

390      GTP is disrupting ER-Golgi trafficking, since this protein was retained and accumulated in the

391      ER when Sar1-GTP was overexpressed, but reached the plasma membrane during GFP and

392      Sar1 overexpression (Fig. 6c).

393
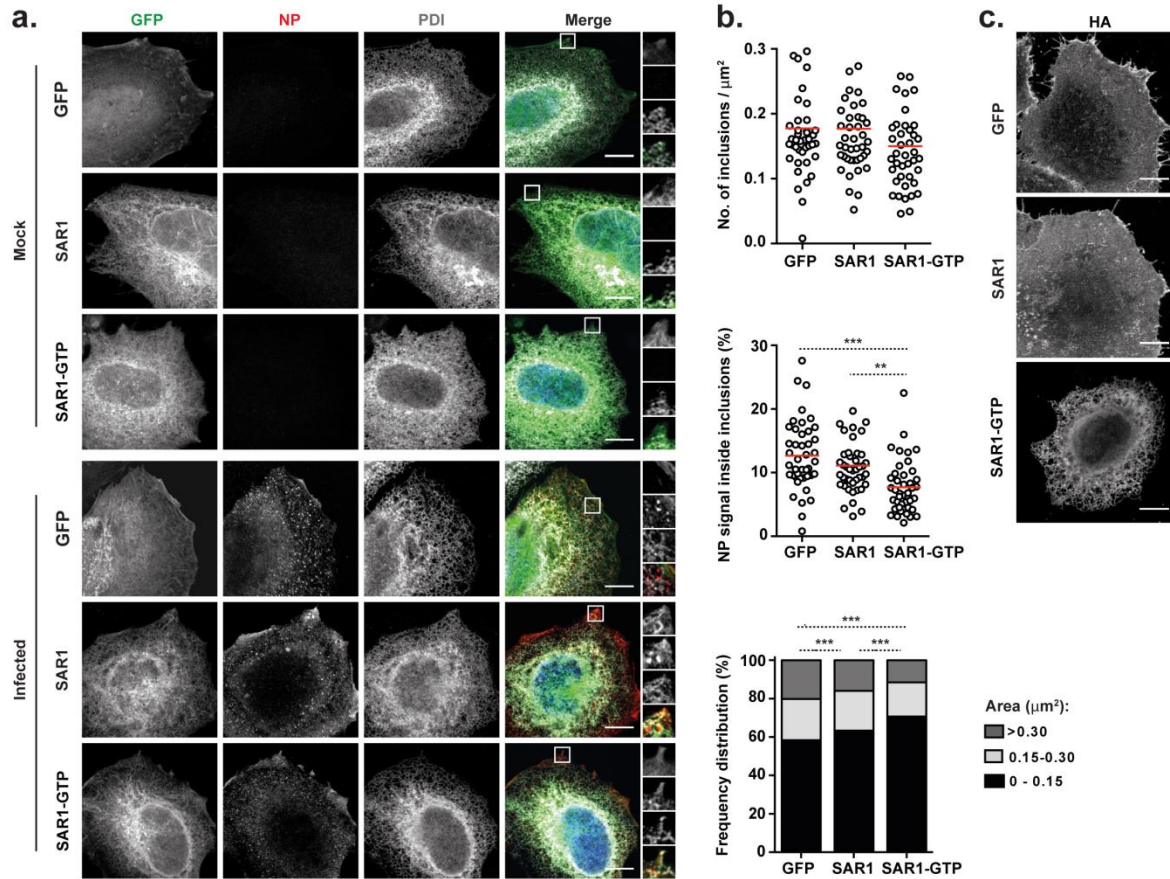
**Figure 6. vRNP clustering is impaired by disruption of ER-exit sites**

HeLa cells were transfected with plasmids encoding GFP, SAR1 WT-GFP or SAR1 GTP-GFP and, 24 h later, infected or mock-infected with PR8 virus, at an MOI of 10. At 16 hpi, cells were fixed and processed for immunofluorescence. **a.** Cells were stained for the viral protein NP (in red) and for the ER protein PDI (in gray). Areas highlighted by the white box are shown on the right of each panel. **b.** The frequency distribution of NP inclusions within the three area categories (in $\mu m^2$), the number of inclusions per $\mu m^2$, and the percentage of NP staining that is inside inclusions were plotted for each condition. Statistical analysis of data was performed using a non-parametric Kruskal–Wallis test, followed by Dunn's multiple comparisons test (***$p < 0.001$). More than 40 cells from 2 independent experiments were analyzed per condition. **c.** Infected cells were stained for the viral protein HA and imaged by confocal microscopy. Bar = 10 $\mu m$.

The above results suggest that the establishment of viral inclusions may also require the Golgi compartment. To address this issue, we inhibited the shuttling of cargo proteins between

21

407    the Golgi and the ER by treating cells with brefeldin A (BFA)[53,54]. Upon addition of a low dosage

408    of BFA to cells infected for 8 h, viral inclusions disassembled within less than 1 hour (Fig. 7a,

409    lower panel). There was a robust and statistically significant decrease in the size [from 0.242 ±

410    0.203 $\mu m^2$ (mean ± SD) to 0.189 ± 0.154 $\mu m^2$, p<0.0001] and number of viral inclusions per $\mu m^2$

411    (from 0.264 ± 0.051 to 0.179 ± 0.056, p<0.0001), as well as in the percentage of NP that was

412    inside the inclusions (from 17.5 ± 4.8 to 9.2 ± 2.8%, p<0.0001) (Fig. 7b). Immunostaining of cells

413    with ER and Golgi makers (PDI and GM310, respectively) revealed that BFA treatment

414    provoked the disassembly of the Golgi complex, as expected[53,54], but not of the ER (Fig. 7a).

415    Areas stained for Rab11 also decreased with BFA treatment (Fig. 7c). Note that the viral

416    transmembrane protein M2 still localized at the plasma membrane, likely because of low dosage

417    (2 $\mu g/mL$) and short duration (1 h) of the BFA treatment (Fig. 7c)[53,54]. In sum, the data

418    collectively shows that biogenesis of IAV liquid viral inclusions enriched in vRNPs and Rab11 is

419    dependent on continuous cycles of material between the ER and the Golgi, indicating that its

420    distribution is spatially regulated.
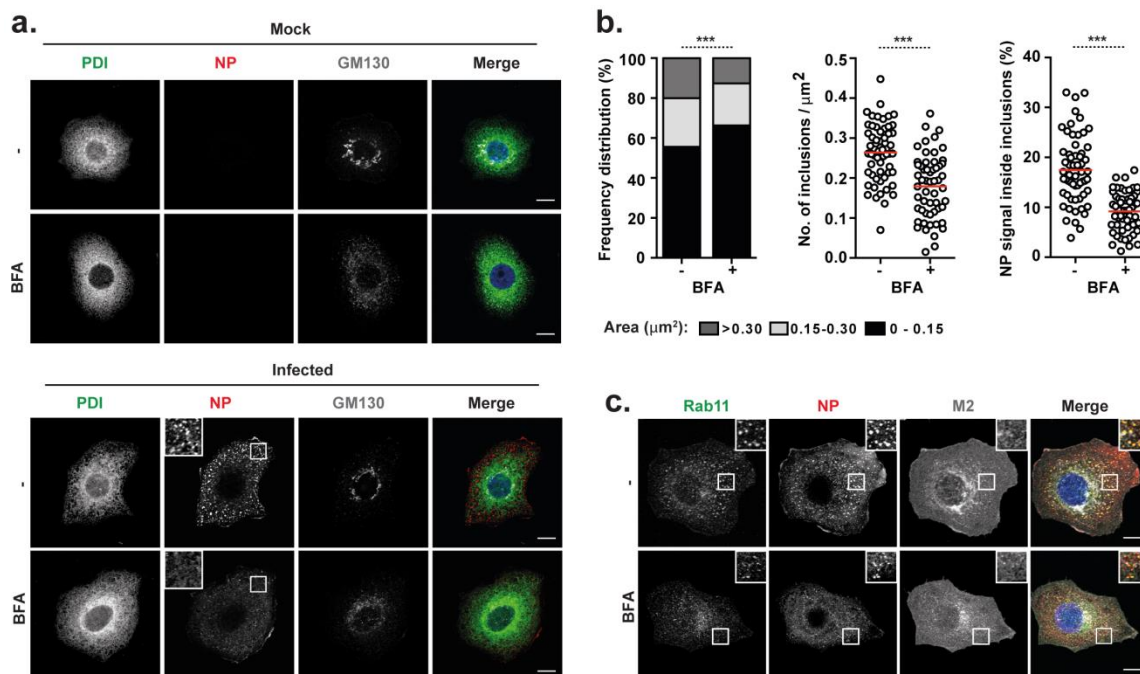


421

422    **Figure 7. Disruption of ER-Golgi trafficking disassembles vRNP hotspots.**

423    A549 cells were infected or mock-infected with PR8 virus at an MOI of 3 for 8 h, and then treated or mock-treated

424    with 2 $\mu$g/mL of brefeldin A (BFA) for 1h. **a.** Cells were immunostained for the ER marker PDI (in green), the viral

425    protein NP (in red) and the cis-Golgi marker GM130 (in gray) and imaged by confocal microscopy. Selected areas of

426    the cytoplasm are marked by white boxes and displayed on the top left corner of the images. Bar = 10 $\mu$m. **b.** The

427    frequency distribution of NP inclusions within the three area categories (in $\mu m^2$), the number of inclusions per $\mu m^2$,

428    and the percentage of NP staining that is inside inclusions were plotted for each condition. Statistical analysis of data

429    was performed using a non-parametric Kruskal–Wallis test, followed by Dunn's multiple comparisons test (***p

430    <0.001). An average of 60 cells from 2 independent experiments was analyzed per condition. **c.** Infected cells were

431    stained for the host protein Rab11 (in green) and the viral proteins NP (in red) and M2 (in gray). Cells were imaged by

432    confocal microscopy. Areas highlighted by the white box are shown on the right top corner of each image. Bar = 10

433    $\mu$m.

434

435    **Discussion**

436    Phase separation by liquid demixing drives functional compartmentalization in cells. It

437    allows the dynamic isolation of sets of selected molecules[35] to carry out activities separated

438    from the surroundings without the need of a membrane[55]. Many membraneless organelles, as

439    the nucleolus[33] and centrosomes[34], constitutively exist in the cell, while others appear after an

440    insult, as stress granules[36], DNA repair foci[56] or G bodies[57].These organelles are beginning to

441    be accepted as a disseminated biological fast adaptation mechanism to respond to stimuli[36,56-58].

442    How viruses take advantage of these phenomena is unclear, despite decades have passed

443    since the realization that many infected cells display viral-induced membraneless territories

444    associated with viral replication, viral assembly, and host immune escape[24,28,29,42].

445    Here, we report that IAV leads to formation of cytosolic inclusions with liquid-like

446    properties (Figs. 1 and 2). They have similar physical characteristics to those found in rabies

447    virus-infected cells in terms of shape, dynamism and ability to deform[43], but are not involved in

448    viral replication as it takes place in the host cell nucleus. In addition, these structures also share

449    properties with other reported liquid bodies including reacting fast to physiological changes[31,59].

450   Formation of these condensates during IAV infection is dependent on Rab11-GTP and on

451   vRNPs. Despite the common characteristics of the molecules involved in IAV inclusion bodies

452   with those described for other membraneless bodies, including multivalency (Rab11)[60,61],

453   internally disordered regions (NP)[31,62], nucleic acids (vRNPs)[63], and oligomerizing RNA binding

454   proteins (NP)[64], the rules underlying the formation of IAV liquid organelles and their functions

455   are far from understood.

456       The IAV-induced inclusions were postulated to originate as vRNPs travelling through the

457   cytosol on Rab11 membranes collided, establishing RNA-RNA interactions *in trans*. Inclusions

458   would contain partial to fully assembled genomes[6,11,13,23]. In this work, we provide evidence that

459   viral inclusions are formed with one vRNP (Fig. 3), which indicates that their formation precedes

460   viral assembly. This supports the idea that viral inclusions could operate as dedicated spots in

461   the cytosol to facilitate establishment of RNA-RNA interactions among the eight different

462   segments. This model still accommodates the hypothesis that vesicular collision could drive

463   genome assembly and is consistent with a selective process for assembling the supra-

464   molecular genomic complex. However, as depicted in the model of Figure 8, these interactions

465   would be restricted in space, taking place in viral inclusions rather than the entire cytosol, and a

466   constant exchange of material between different viral inclusions would replenish vRNP stocks

467   and remove fully assembled genomes by an unclear process. Nevertheless, for the exchange of

468   material to occur, viral inclusions need to move.

469

470
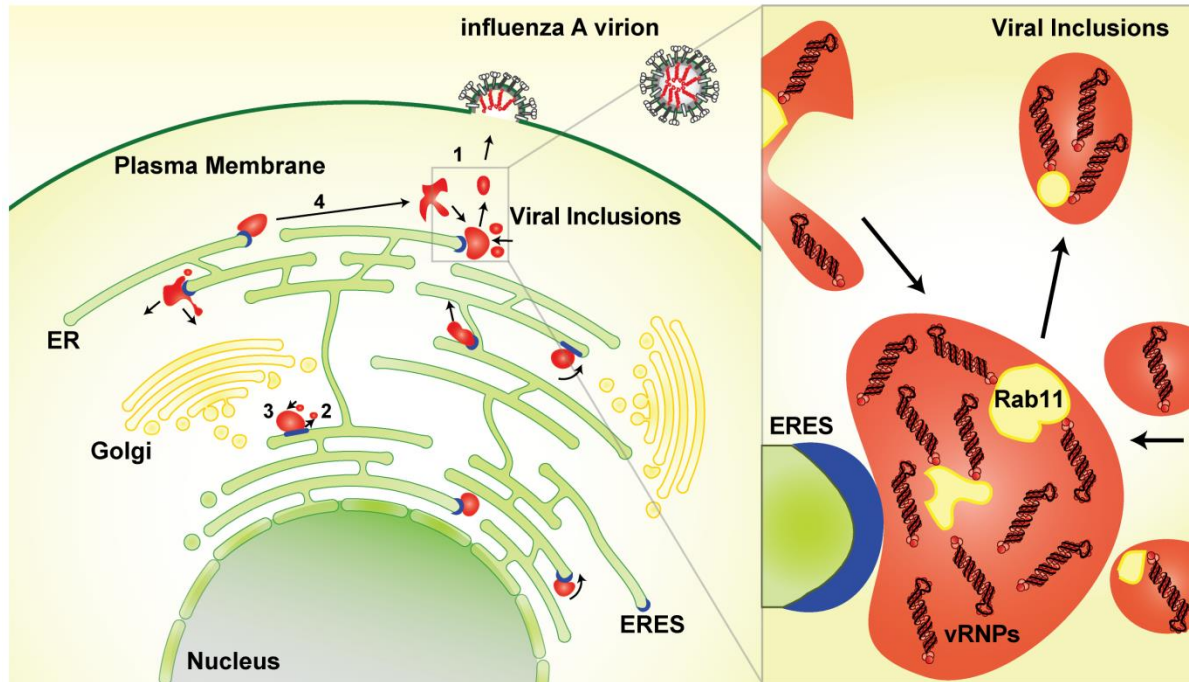
**Figure 8. Proposed model**

Viral inclusions (in red) exhibit characteristics of liquid organelles, segregating from the cytosol without a delimitating membrane. Viral inclusions exchange material dynamically (1) and deform easily exhibiting fission (2) and fusion (3) events. Viral inclusions can travel long distances before and after fusion/fission events (4), respectively. These organelles are formed in the vicinity of ERES (in blue) and their assembly is dependent on continuous ER-Golgi vesicular cycling. We propose that viral inclusions trigger nucleation of RNA-RNA interactions among the eight different segments to assemble a complete IAV genome. Inlet shows composition of viral inclusions close to ERES. These contain vRNPs of all types, Rab11 and host membranes clustered, but are not delimited by lipid bilayer.

Our work indicates a cross-talk between molecular motors and viral inclusions, with different viral inclusions fusing or dividing in a manner dependent of sheer force (Fig. 2). In addition, IAV Rab11/vRNPs hotspots were shown to exhibit heterogeneous movements, as if moving on actin or sliding on microtubules[10,17,30], using molecular motors[65]. However, it was recently reported that, in the absence of intact microtubules, vRNAs could be transported through the cytoplasm independently of Rab11-GTP[66] and a candidate that was recently proposed was the ER[16]. Our work shows, using distinct ways, that molecular crowding occurs in

25

487    the vicinity of ERES (Fig. 5) and is dependent on continuous vesicular cycling between ER and

488    Golgi (Figs. 6 and 7). This suggests that inclusion formation is spatially regulated. In fact, the

489    movement of IAV inclusions matches that of the ER (Fig. 5) and, in some cases, inclusions

490    seem to slide on ER membranes (Supplementary Movies 7 and 8). This raises the possibility

491    that viral inclusions move gliding through the ER. This notion is in agreement with vRNPs being

492    found at the ER[16]. Interestingly, biogenesis of viral inclusions seems to be intertwined with

493    deregulation of the ERC, which is coherent with a decrease in recycling of transferrin during

494    infection[14,21], and with Rab11 detection in the ER, as if it was re-directed to this organelle during

495    infection[16]. Whether Rab11 vesicles are targeted to the ER to deliver or to collect vRNPs will be

496    addressed in the future. Inhibiting ER-Golgi vesicle cycles has efficiently locked HA, but not

497    vRNPs, in the ER (Figs. 6 and 7), which supports the former hypothesis, but more experiments

498    are necessary to validate one model. In both cases, there are unresolved questions regarding:

499    1) the transport of vRNPs to or from the ER; 2) the selection of the ERES as docking sites for

500    viral inclusions and 3) the sensing and transport of fully assembled genomes to the plasma

501    membrane.

502        Nevertheless, for several biological systems, an intimate association between RNA and

503    liquid membraneless organelles has been reported[57,67-69]. In some cases, RNA promotes phase

504    separation[57,67], while in other it inhibits this process[68,69]. Many membraneless organelles are

505    involved in RNA metabolism, as is the case of Cajal bodies, nucleoli or stress granules, and

506    therefore it is not surprising that liquid bodies could be involved in IAV genome assembly.

507    Phase separation could however play other roles during IAV infection. We found no differences

508    in the activation of IFN response when viral inclusion assembly was inhibited (Fig. 4), but we

509    have not tested exhaustively other immune related parameters. IAV-induced phase separation

510    leads to localized concentration of vRNPs and many proteins (some possibly unidentified). As

511    shown for other systems, it could operate in signal amplification[70] or repression/activation of

512    specific cellular pathways by exclusion/inclusion of selected molecules[71].

26

513    Although we favor involvement in viral assembly by spatially restricting vRNPs and

514    facilitate interactions, compelling evidence is required to formally validate this model.

515    Importantly, future experiments will have to detail the internal organization of the viral inclusions.

516    In particular, whether different vRNPs define physical cross-links and establish differences in

517    the property of the material, leading to spatial organization, or alter the diffusion/movement

518    within inclusions, remains to be seen. Besides spatial organization, other factors affecting liquid

519    properties include molecular crowding, solubility affinity or the valency of phase-separating

520    proteins[71] and these could fluctuate during the course of infection. We are just beginning to

521    understand the involvement of liquid-liquid phase separation in virology, but we anticipate that,

522    given the ancient co-evolution between viruses and eukaryotic cells, and the diversity of host

523    strategies used by viruses, the next years will provide an interesting overlap between the two

524    fields.

525

526    **METHODS**

527    **Cells, Viruses and Drugs.** The human epithelial cells Madin-Darby Canine Kidney (MDCK),

528    embryonic kidney 293T, cervical HeLa and alveolar basal (A549) were a kind gift of Prof Paul

529    Digard, Roslin Institute, UK. The GFP-Rab11 WT and GFP-Rab11 DN (A549) were produced by

530    our laboratory[14]. The Sec61β-Emerald (HeLa) cell line was a kind gift from Dr Christoph Dehio,

531    Biozentrum, University of Basel, Switzerland[47,72]. All cell types were cultured as described

532    before[10] and were regularly tested for mycoplasma contamination with the LookOut

533    mycoplasma PCR detection kit (Sigma, MP0035), using JumpStart Taq DNA Polymerase

534    (Sigma, D9307). Reverse-genetics derived A/Puerto Rico/8/34 (PR8 WT; H1N1) was used as a

535    model virus and titrated according to reference[14]. NS1 N81 mutant virus was derived from PR8

536    WT and expresses only the first 81 amino acids of NS1[44]. Reverse genetic plasmids were

537    contributed by Dr Ron Fouchier, Erasmus MC, Netherlands. Virus infections were performed at

538    a multiplicity of infection (MOI) of 3 to 10. After 45 min, cells were overlaid with DMEM

27

539  containing 10% fetal bovine serum (Gibco, Life Technologies, 10500-064) and 1% penicillin /

540  streptomycin mix (Biowest, L0022-100). The drug brefeldin A (Sigma) was dissolved in ethanol

541  and used at final concentration of 2 $\mu$g/ml.

542

543  **Plasmids.** HA tagged Sec23 plasmid was a kind gift from Dr Colin Adrain, IGC, Portugal. GFP

544  tagged Sec16 plasmid was purchased from Addgene. GFP-Sec61$\beta$ was constructed by PCR-

545  amplifying Sec61$\beta$ from A549 cDNA and cloning it into pEGFP-C2, using *Hin*dIII and *Kpn*I

546  restriction sites. Sar1A was amplified from A549 cDNA and cloned *Xho*I-*Bam*HI restriction sites

547  of pEGFP-N1. GTP-restricted SAR1 (H79G) was produced by site-directed mutagenesis from

548  SAR1 WT-GFP. ER-GFP plasmid was made from pEGFP-C2, by inserting a C-terminal KDEL

549  sequence by site-directed mutagenesis, and an N-terminal ER-signal sequence from calreticulin

550  by oligo-annealing between *Nhe*I and *Age*I restriction sites. Plasmids used for the minireplicon

551  system have been described in reference[10], except pcDNA3-NS2. The latter was made by PCR

552  amplification of NS2 (from PR8) and insertion into pCDNA3, using *Eco*RI and *Not*I restriction

553  sites. The following primers/oligos were used:

554  Sec61$\beta$ Fw: 5'-TAGAAAGCTTCATGCCTGGTCCGACCC-3'

555  Sec61$\beta$ Rv: 5'-TCGAGGTACCCTACGAACGAGTGTACTTGCCC-3'

556  SAR1 WT Fw: 5'- TCGACTCGAGATGTCTTTCATCTTTGAGTGGATCT- 3'

557  SAR1 WT Rv: 5'- TCGAGGATCCCGGTCAATATACTGGGAGAGCCAGC- 3'

558  SAR1 H79G FW: 5'- TTTTGATCTTGGTGGGGGCGAGCAAGCACGTCGC - 3'

559  SAR1 H79G RV: 5'- GCGACGTGCTTGCTCGCCCCCACCAAGATCAAAA - 3'

560  KDEL Fw: 5'-TGGACGAGCTGTACAAGGACGAGCTGTAATCCGGCCGGACT-3'

561  KDEL Rv: 5'- AGTCCGGCCGGATTACAGCTCGTCCTTGTACAGCTCGTCCA-3'

562  Calreticulin tag up: 5'-

563  CTAGCATGCTGCTATCCGTGCCGTTGCTGCTCGGCCTCCTCGGCCTGGCCGTCGCA-3'

28

564     Calreticulin tag down: 5'-

565     CCGGTGCGACGGCCAGGCCGAGGAGGCCGAGCAGCAACGGCACGGATAGCAGCATG-3'

566     NS2 Fw:  5'-CGTAGCGAATTCATGGATCCAAACACTG-3'

567     NS2 Rv: 5'-GCTAAGACGCGGCCGCTTAAATAAGCTGAAAC-3'

568

569     **Transfections.** Cells, grown to 70% confluency in 24 well plates, were transfected with 250 ng

570     of indicated plasmids or 100 ng of the synthetic dsRNA polyinosinic:polycytidylic acid [poly(I:C);

571     Calbiochem], using Lipofectamine LTX (Life Technologies) and Opti-MEM (Life Technologies),

572     according to manufacturer's instructions. Cells were infected or mock-infected 16 h post-

573     transfection or simultaneously with transfection (live-cell imaging) at indicated MOI.

574     To reconstitute GFP-tagged RNPs, 293T cells grown to 70% confluency in 24 well plates were

575     transfected with plasmids pcDNA PB1, PB2, PA (130 ng each), NP (150 ng), GFP-NP (50 ng),

576     pPol I segments 7 and 8 (130 ng each) or/and pcDNA-NS2, using Lipofectamine 2000

577     (Invitrogen) according to the manufacturer's instructions, incubated overnight, and imaged

578     around 12-16 h later.

579

580     **Confocal fixed-cell imaging.** Fluorescent *in situ* hybridization (FISH) assay was done as in[10].

581     Immunofluorescence assays were performed as in[10]. Antibodies used were: rabbit polyclonal

582     against Rab11a (1:100; Life Technologies, 715300), HA tag (1:500; Abcam, 9110), calnexin

583     (1:1000, Abcam, 22595), atlastin 3 (1:100; Proteintech, 16921-1-AP) and NP (1:1000; gift from

584     Prof Paul Digard); mouse monoclonal against NP (1:1000; Abcam, 20343), virus HA (neat; gift

585     from Prof Paul Digard), M2 (1:500, Abcam, 5416), PDI (1:500, Life Technologies, MA3-019) and

586     Sec31A (1:100; BD Biosciences, 612350); goat polyclonal against ERp57 (1:200; Sicgen,

587     AB0003-200). Secondary antibodies were all from the Alexa Fluor range (1:1000; Life

588     Technologies). Single optical sections were imaged with a Leica SP5 live confocal microscope.

589     Cluster size was quantified as published previously[14]. Distributions (in %) were calculated and

29

590    plotted by GraphPad Prism. Images were post-processed using Adobe Photoshop CS5 and

591    ImageJ (NIH).

592

593    **Live cell imaging.** Cells were grown in chambered glass-bottomed dishes (Lab-Tek) and

594    maintained at 37°C in Leibovitz L-15 $CO_2$-independent medium (Gibco) during imaging.

595    Samples were imaged using Leica SP5 Inverted or Roper TIRF Spinning Disk (Yokogawa CSU-

596    X1) and post-processed using Adobe Photoshop CS5 and ImageJ (NIH).

597    For fluorescence recovery after photobleaching (FRAP) analysis, cells were transfected with

598    250 ng of GFP-NP and immediately superinfected with PR8 at an MOI of 10. At 12 hpi, media

599    was substituted for Leibovitz L-15 media to buffer $CO_2$ and data acquisition started on a Roper

600    TIRF Spinning Disk (Yokogawa CSU-X1) with a cage incubator to control temperature at 37 ºC.

601    After excitation with a 491 nm laser (Cobolt 491, 100 mW), fluorescence from GFP was

602    detected with a 100x oil immersion objective (Plan Apo 1.49), a bandpass filter (525/45

603    Chroma), and a photometrics 512 EMCCD camera. All FRAP experiments were performed

604    similarly using iLas FRAP module (Rope Scientific): 2 sec prebleach, 12.18 msec/$\mu m^2$ bleach,

605    60 sec postbleach at a frame rate of 3 images per second. Bleaching was performed in a

606    variable circular area to target complete viral inclusions. For FRAP analysis, samples were

607    corrected for background fluorescence and acquisition photobleaching as described previously

608    by the Phair method[73]. After normalization, FRAP curves were fitted following the exponential

609    function: Y=Y0 + (Plateau-Y0)*(1-exp(-D*x)), where:

610    Y0: Y value when X (time) is zero. It is expressed in the same units as Y.

611    Plateau (must be less than one): Y value at infinite times, expressed in the same units as Y. D:

612    rate constant, expressed in reciprocal of the X axis time units.

613    Tau: time constant, expressed in the same units as the X axis. It is computed as the reciprocal

614    of D.

615    Half-time: time units of the X axis. It is computed as ln(2)/D.

30

616     Span (mobile phase): difference between Y0 and Plateau, expressed in the same units as your

617     Y values.

618

619     **Tokuyasu – Double Immunogold labeling.** Cells infected with PR8, at an MOI of 5, were fixed

620     in suspension using 2% (v/v) formaldehyde (EMS) and 0.2% (v/v) glutaraldehyde (Polysciences)

621     in 0.1 M Phosphate buffer (PB), for 2 h at RT. Subsequently, cells were centrifuged and washed

622     with PB. The aldehydes were quenched using 0.15% (w/v) glycine (VWR) in 0.1 M PB for 10

623     min at RT. Cells were infiltrated in 12% (w/v) gelatin (Royal) for 30 min at 37ºC and centrifuged.

624     The gelatin was solidified on ice, cut into 1 mm$^3$ cubes and placed in 2.3 M sucrose (Alfa Aesar)

625     in 0.1 M PB, ON at 4ºC. The cubes were mounted onto specimen holders and frozen at -196ºC

626     by immersion into liquid nitrogen. Samples were trimmed and cut into 50 nm-thick sections (in a

627     Leica EM-FC7 at -110ºC) and laid onto formvar-carbon coated 100-mesh grids.

628     For immunogold labeling, sections were blocked with PBS/1% BSA for 20 min at RT. Antibody

629     staining was done sequentially in PBS/1% BSA at RT: rabbit anti-GFP (1:500, 1 h), goat anti-

630     rabbit IgG conjugated to 18 nm-gold (1:20, 30 min), mouse anti-NP (1:200, 1 h) and goat anti-

631     mouse IgG conjugated with 6 nm-gold (1:20, 30 min). Gold particles were fixed by applying 1%

632     (v/v) formaldehyde in PBS for 5 min at RT. Blocking and extensive washing were performed in-

633     between stainings. In the final step, gold particles were fixed using 1% (v/v) glutaraldehyde

634     (Polysciences) for 5 min RT. Grids were washed in distilled $H_2O$ and counterstained using

635     methyl-cellulose–uranyl acetate solution for 5 min on ice. EM images were acquired on a Hitachi

636     H-7650 operating at 100 keV equipped with a XR41M mid mount AMT digital camera. Images

637     were post-processed using Adobe Photoshop CS5 and ImageJ (NIH).

638

639     **Correlative light and electron microscopy (CLEM).** Cells, seeded onto gridded dishes

640     (MatTek Corporation, P35G-2-14-C-GRID), were transfected with GFP-NP and simultaneously

641     infected or mock-infected with PR8 at an MOI of 10. At indicated times, cells were fixed, imaged

31

642  at the confocal microscope Leica SP5 Inverted and finally processed for electron microscopy

643  imaging, as described previously[14]. Sections of 70 nm thickness were cut using a Leica EM-FC7

644  Ultramicrotome. The regions of interest were acquired with a Hitachi H-7650 operating at 100

645  keV equipped with a XR41M mid mount AMT digital camera. Images were post-processed using

646  Adobe Photoshop CS5 and ImageJ (NIH).

647

648  **Western blotting.** Western blotting was performed according to standard procedures and

649  imaged using a LI-COR Biosciences Odyssey near-infrared platform as in[45]. Antibodies used

650  included: rabbit polyclonal against pIRF3 (1:1000; Cell Signal, 4947), virus NP (1:1000), PB1,

651  PB2, PA and NS1 (all at 1:500), kindly provided by Prof. Paul Digard, Roslin Institute, UK; goat

652  polyclonal against green fluorescent protein (GFP) (1:2000; Sicgen, AB0020), GAPDH (1:2000;

653  Sicgen, AB0049) and virus M1 (1:500; Abcam, 20910); mouse polyclonal against virus M2

654  (1:500; Abcam, 5416). The secondary antibodies used were from IRDye range (1:10000; LI-

655  COR Biosciences).

656

657  **Enzyme-linked immunosorbent assay.** Detection of IFN-$\beta$ in the cell supernatants was done

658  using the Verikine[TM] Human IFN Beta ELISA kit (PBL Assay Science, 41410), range 50-4000

659  pg/mL, following the manufacturer's instructions.

660

661  **Quantitative real-time reverse-transcription PCR (RT-qPCR).** Extraction of RNA from

662  samples in NZYol (NZYtech, MB18501) was achieved by using the Direct-zol RNA minipreps

663  (Zymo Research, R2052). Reverse transcription (RT) was performed using the transcriptor first

664  strand cDNA kit (Roche, 04896866001). Real-time RT-PCR to detect GAPDH and IFN- $\beta$, IFN-

665  $\alpha$, IL-29 and Viperin was prepared in 384-well, white, thin walled plates (Biorad, HSP3805) by

666  using SYBR Green Supermix (Biorad, 172-5124), 10% (v/v) of cDNA and 0.4 $\square$M of each

667    primer. The reaction was performed on a CFX 384 Touch Real-Time PCR Detection System

668    machine (Biorad), under the following PCR conditions: Cycle 1 (1 repeat): 95°C for 2 min; Cycle

669    2 (40 repeats): 95°C for 5 s and 60°C for 30 s; Cycle 3: 95°C for 5 s and melt curve 65°C to

670    95°C (increment 0.05°C each 5 s). Data were analysed using the CFX manager software

671    (Biorad).

672    Primer sequenced used for real-time RT-qPCR were the following:

673    GAPDH Fw: 5′-CTCTGCTCCTCCTGTTCGAC-3′;

674    GAPDH Rv: 5′-ACCAAATCCGTTGACTCCGAC-3′;

675    IL-29 Fw: 5'-AATTGGGACCTGAGGCTTCT-3';

676    IL-29 Rv: 5'- GTGAAGGGGCTGGTCTAGGA-3';

677    IFN-β Fw: 5'- CCTGAAGGCCAAGGAGTACA-3';

678    IFN-β Rv: 5'- AAGCAATTGTCCAGTCCCAG-3'

679    IFN-α Fw: 5'- ATGGCCCTGTCCTTTTCTTT-3'

680    IFN-α Rv: 5'- ATTCTTCCCATTTGTGCCAG-3'

681    Viperin Fw: 5'- TCACTCGCCAGTGCAACTAC-3'

682    Viperin Rv: 5'- TGGCTCTCCACCTGAAAAGT-3'

683

684    **ACKNOWLEDGEMENTS**

692    Netherlands) for the reverse genetics plasmids, Dr Colin Adrain (IGC, Portugal) for Sec23

693    plasmid, and Dr Christoph Dehio for Sec61β-Emerald cell line (University of Basel, Switzerland).

694    The authors thank Dr Fabrice Cordelières from the Bordeaux Imaging Center (INSERM,

695    France), Gabriel Martins (IGC, Portugal), Nuno Pimpão (IGC, Portugal) and Dr Luís Moita (IGC,

696    Portugal) for helpful discussion.

697

698    **AUTHOR CONTRIBUTIONS**

699    MJA, MA, SVC designed the experiments; all authors carried out experiments and analyzed the

700    data; MJA supervised the research and conceived the experiments; MJA, MA and SVC wrote

701    the manuscript; all authors contributed to editing the manuscript.

702

703    **COMPETING INTERESTS**

704    The authors declare no competing interests

705

706    **REFERENCES**

707    1    Kumar, B. *et al.* The emerging influenza virus threat: status and new prospects for its therapy and control. *Arch*
708         *Virol* **163**, 831-844, doi:10.1007/s00705-018-3708-y (2018).
709    2    Lee, N. *et al.* Genome-wide analysis of influenza viral RNA and nucleoprotein association. *Nucleic Acids Res* **45**,
710         8968-8977, doi:10.1093/nar/gkx584 (2017).
711    3    Lowen, A. C. Constraints, Drivers, and Implications of Influenza A Virus Reassortment. *Annu Rev Virol* **4**, 105-121,
712         doi:10.1146/annurev-virology-101416-041726 (2017).
713    4    Belshaw, R., Gardner, A., Rambaut, A. & Pybus, O. G. Pacing a small cage: mutation and RNA viruses. *Trends*
714         *Ecol Evol* **23**, 188-193, doi:10.1016/j.tree.2007.11.010 (2008).
715    5    Ferhadian, D. *et al.* Structural and Functional Motifs in Influenza Virus RNAs. *Front Microbiol* **9**, 559,
716         doi:10.3389/fmicb.2018.00559 (2018).
717    6    Giese, S., Bolte, H. & Schwemmle, M. The Feat of Packaging Eight Unique Genome Segments. *Viruses* **8**,
718         doi:10.3390/v8060165 (2016).
719    7    Fournier, E. *et al.* Interaction network linking the human H3N2 influenza A virus genomic RNA segments. *Vaccine*
720         **30**, 7359-7367, doi:10.1016/j.vaccine.2012.09.079 (2012).
721    8    Gavazzi, C. *et al.* An in vitro network of intermolecular interactions between viral RNA segments of an avian H5N2
722         influenza A virus: comparison with a human H3N2 virus. *Nucleic Acids Res* **41**, 1241-1254,
723         doi:10.1093/nar/gks1181 (2013).
724    9    Nakatsu, S. *et al.* Complete and Incomplete Genome Packaging of Influenza A and B Viruses. *MBio* **7**,
725         doi:10.1128/mBio.01248-16 (2016).
726    10   Amorim, M. J. *et al.* A Rab11- and microtubule-dependent mechanism for cytoplasmic transport of influenza A
727         virus viral RNA. *J Virol* **85**, 4143-4156, doi:JVI.02606-10 [pii] 10.1128/JVI.02606-10 (2011).
728    11   Chou, Y. Y. *et al.* Colocalization of different influenza viral RNA segments in the cytoplasm before viral budding as
729         shown by single-molecule sensitivity FISH analysis. *PLoS Pathog* **9**, e1003358, doi:10.1371/journal.ppat.1003358
730         (2013).
731    12   Eisfeld, A. J., Kawakami, E., Watanabe, T., Neumann, G. & Kawaoka, Y. RAB11A is essential for transport of the
732         influenza virus genome to the plasma membrane. *J Virol* **85**, 6117-6126, doi:JVI.00378-11 [pii] 10.1128/JVI.00378-
733         11 (2011).

13    Lakdawala, S. S. *et al.* Influenza a virus assembly intermediates fuse in the cytoplasm. *PLoS Pathog* **10**, e1003971, doi:10.1371/journal.ppat.1003971
      PPATHOGENS-D-13-02311 [pii] (2014).

14    Vale-Costa, S. *et al.* Influenza A virus ribonucleoproteins modulate host recycling by competing with Rab11 effectors. *J Cell Sci* **129**, 1697-1710, doi:10.1242/jcs.188409 (2016).

15    Vale-Costa, S. & Amorim, M. J. Clustering of Rab11 vesicles in influenza A virus infected cells creates hotspots containing the eight viral ribonucleoproteins. *Small GTPases*, 0, doi:10.1080/21541248.2016.1199190 (2016).

16    de Castro Martin, I. F. *et al.* Influenza virus genome reaches the plasma membrane via a modified endoplasmic reticulum and Rab11-dependent vesicles. *Nat Commun* **8**, 1396, doi:10.1038/s41467-017-01557-6 (2017).

17    Momose, F. *et al.* Apical Transport of Influenza A Virus Ribonucleoprotein Requires Rab11-positive Recycling Endosome. *PLoS One* **6**, e21123, doi:PONE-D-11-05025 [pii] 10.1371/journal.pone.0021123 (2011).

18    Vale-Costa, S. & Amorim, M. J. Recycling Endosomes and Viral Infection. *Viruses* **8**, doi:10.3390/v8030064 (2016).

19    Avilov, S. V. *et al.* Replication-competent influenza A virus that encodes a split-green fluorescent protein-tagged PB2 polymerase subunit allows live-cell imaging of the virus life cycle. *J Virol* **86**, 1433-1448, doi:10.1128/JVI.05820-11 (2012).

20    Hutchinson, E. C. *et al.* Conserved and host-specific features of influenza virion architecture. *Nat Commun* **5**, 4816, doi:10.1038/ncomms5816 (2014).

21    Kawaguchi, A., Hirohama, M., Harada, Y., Osari, S. & Nagata, K. Influenza Virus Induces Cholesterol-Enriched Endocytic Recycling Compartments for Budozone Formation via Cell Cycle-Independent Centrosome Maturation. *PLoS Pathog* **11**, e1005284, doi:10.1371/journal.ppat.1005284 (2015).

22    Hutchinson, E. C. & Fodor, E. Transport of the influenza virus genome from nucleus to nucleus. *Viruses* **5**, 2424-2446, doi:10.3390/v5102424 (2013).

23    Lakdawala, S. S., Fodor, E. & Subbarao, K. Moving On Out: Transport and Packaging of Influenza Viral RNA into Virions. *Annu Rev Virol* **3**, 411-427, doi:10.1146/annurev-virology-110615-042345 (2016).

24    Netherton, C., Moffat, K., Brooks, E. & Wileman, T. A guide to viral inclusions, membrane rearrangements, factories, and viroplasm produced during virus replication. *Adv Virus Res* **70**, 101-182, doi:10.1016/S0065-3527(07)70004-0 (2007).

25    Netherton, C. L. & Wileman, T. Virus factories, double membrane vesicles and viroplasm generated in animal cells. *Curr Opin Virol* **1**, 381-387, doi:10.1016/j.coviro.2011.09.008 (2011).

26    Wileman, T. Aggresomes and pericentriolar sites of virus assembly: cellular defense or viral design? *Annu Rev Microbiol* **61**, 149-167, doi:10.1146/annurev.micro.57.030502.090836 (2007).

27    Nikolic, J. *et al.* Negri bodies are viral factories with properties of liquid organelles. *Nat Commun* **8**, 58, doi:10.1038/s41467-017-00102-9 (2017).

28    Rhim, J. S., Jordan, L. E. & Mayor, H. D. Cytochemical, fluorescent-antibody and electron microscopic studies on the growth of reovirus (ECHO 10) in tissue culture. *Virology* **17**, 342-355 (1962).

29    Morgan, C., Ellison, S. A., Rose, H. M. & Moore, D. H. Structure and development of viruses observed in the electron microscope. II. Vaccinia and fowl pox viruses. *J Exp Med* **100**, 301-310 (1954).

30    Amorim, M. J., Kao, R. Y. & Digard, P. Nucleozin targets cytoplasmic trafficking of viral ribonucleoprotein-rab11 complexes in influenza a virus infection. *J Virol* **87**, 4694-4703, doi:10.1128/JVI.03123-12 (2013).

31    Nott, T. J. *et al.* Phase transition of a disordered nuage protein generates environmentally responsive membraneless organelles. *Mol Cell* **57**, 936-947, doi:10.1016/j.molcel.2015.01.013 (2015).

32    Hyman, A. A., Weber, C. A. & Julicher, F. Liquid-liquid phase separation in biology. *Annu Rev Cell Dev Biol* **30**, 39-58, doi:10.1146/annurev-cellbio-100913-013325 (2014).

33    Feric, M. *et al.* Coexisting Liquid Phases Underlie Nucleolar Subcompartments. *Cell* **165**, 1686-1697, doi:10.1016/j.cell.2016.04.047 (2016).

34    Woodruff, J. B. *et al.* The Centrosome Is a Selective Condensate that Nucleates Microtubules by Concentrating Tubulin. *Cell* **169**, 1066-1077 e1010, doi:10.1016/j.cell.2017.05.028 (2017).

35    Brangwynne, C. P. *et al.* Germline P granules are liquid droplets that localize by controlled dissolution/condensation. *Science* **324**, 1729-1732, doi:10.1126/science.1172046 (2009).

36    Molliex, A. *et al.* Phase separation by low complexity domains promotes stress granule assembly and drives pathological fibrillization. *Cell* **163**, 123-133, doi:10.1016/j.cell.2015.09.015 (2015).

37    Essere, B. *et al.* Critical role of segment-specific packaging signals in genetic reassortment of influenza A viruses. *Proc Natl Acad Sci U S A* **110**, E3840-3848, doi:10.1073/pnas.1308649110 (2013).

38    Gavazzi, C. *et al.* A functional sequence-specific interaction between influenza A virus genomic RNA segments. *Proc Natl Acad Sci U S A* **110**, 16604-16609, doi:10.1073/pnas.1314419110 (2013).

39    Venev, S. V. & Zeldovich, K. B. Segment self-repulsion is the major driving force of influenza genome packaging. *Phys Rev Lett* **110**, 098104, doi:10.1103/PhysRevLett.110.098104 (2013).

40    Duhaut, S. D. & McCauley, J. W. Defective RNAs inhibit the assembly of influenza virus genome segments in a segment-specific manner. *Virology* **216**, 326-337, doi:10.1006/viro.1996.0068 (1996).

41    Inagaki, A., Goto, H., Kakugawa, S., Ozawa, M. & Kawaoka, Y. Competitive incorporation of homologous gene segments of influenza A virus into virions. *J Virol* **86**, 10200-10202, doi:10.1128/JVI.01204-12 (2012).

42    Wu, X. *et al.* Evasion of antiviral immunity through sequestering of TBK1/IKKepsilon/IRF3 into viral inclusion bodies. *J Virol* **88**, 3067-3076, doi:10.1128/JVI.03510-13 (2014).

35

43  Nikolic, J., Civas, A., Lama, Z., Lagaudriere-Gesbert, C. & Blondel, D. Rabies Virus Infection Induces the Formation of Stress Granules Closely Connected to the Viral Factories. *PLoS Pathog* **12**, e1005942, doi:10.1371/journal.ppat.1005942 (2016).

44  Pereira, C. F., Read, E. K. C., Wise, H. M., Amorim, M. J. & Digard, P. Influenza A Virus NS1 Protein Promotes Efficient Nuclear Export of Unspliced Viral M1 mRNA. *J Virol* **91**, doi:10.1128/JVI.00528-17 (2017).

45  Bruce, E. A., Digard, P. & Stuart, A. D. The Rab11 pathway is required for influenza A virus budding and filament formation. *J Virol* **84**, 5848-5859, doi:10.1128/JVI.00307-10 (2010).

46  Garcia-Sastre, A. *et al.* Influenza A virus lacking the NS1 gene replicates in interferon-deficient systems. *Virology* **252**, 324-330 (1998).

47  Nixon-Abell, J. *et al.* Increased spatiotemporal resolution reveals highly dynamic dense tubular matrices in the peripheral ER. *Science* **354**, doi:10.1126/science.aaf3928 (2016).

48  Budnik, A. & Stephens, D. J. ER exit sites--localization and control of COPII vesicle formation. *FEBS letters* **583**, 3796-3803, doi:10.1016/j.febslet.2009.10.038 (2009).

49  Chen, S. *et al.* Lunapark stabilizes nascent three-way junctions in the endoplasmic reticulum. *Proc Natl Acad Sci U S A* **112**, 418-423, doi:10.1073/pnas.1423026112 (2015).

50  Barlowe, C. & Helenius, A. Cargo Capture and Bulk Flow in the Early Secretory Pathway. *Annu Rev Cell Dev Biol* **32**, 197-222, doi:10.1146/annurev-cellbio-111315-125016 (2016).

51  Matsuoka, K. *et al.* COPII-coated vesicle formation reconstituted with purified coat proteins and chemically defined liposomes. *Cell* **93**, 263-275 (1998).

52  Aridor, M. *et al.* The Sar1 GTPase coordinates biosynthetic cargo selection with endoplasmic reticulum export site assembly. *The Journal of cell biology* **152**, 213-229 (2001).

53  Tse, Y. C., Lam, S. K. & Jiang, L. Enigmatic brefeldin a. *Plant Signal Behav* **2**, 199-202 (2007).

54  Wagner, M., Rajasekaran, A. K., Hanzel, D. K., Mayor, S. & Rodriguez-Boulan, E. Brefeldin A causes structural and functional alterations of the trans-Golgi network of MDCK cells. *J Cell Sci* **107 ( Pt 4)**, 933-943 (1994).

55  Banani, S. F., Lee, H. O., Hyman, A. A. & Rosen, M. K. Biomolecular condensates: organizers of cellular biochemistry. *Nat Rev Mol Cell Biol* **18**, 285-298, doi:10.1038/nrm.2017.7 (2017).

56  Altmeyer, M. *et al.* Liquid demixing of intrinsically disordered proteins is seeded by poly(ADP-ribose). *Nat Commun* **6**, 8088, doi:10.1038/ncomms9088 (2015).

57  Jin, M. *et al.* Glycolytic Enzymes Coalesce in G Bodies under Hypoxic Stress. *Cell Rep* **20**, 895-908, doi:10.1016/j.celrep.2017.06.082 (2017).

58  Wheeler, J. R., Matheny, T., Jain, S., Abrisch, R. & Parker, R. Distinct stages in stress granule assembly and disassembly. *Elife* **5**, doi:10.7554/eLife.18413 (2016).

59  Boke, E. *et al.* Amyloid-like Self-Assembly of a Cellular Compartment. *Cell* **166**, 637-650, doi:10.1016/j.cell.2016.06.051 (2016).

60  Li, P. *et al.* Phase transitions in the assembly of multivalent signalling proteins. *Nature* **483**, 336-340, doi:10.1038/nature10879 (2012).

61  Kelly, E. E., Horgan, C. P. & McCaffrey, M. W. Rab11 proteins in health and disease. *Biochemical Society transactions* **40**, 1360-1367, doi:10.1042/BST20120157 (2012).

62  Kakisaka, M., Yamada, K., Yamaji-Hasegawa, A., Kobayashi, T. & Aida, Y. Intrinsically disordered region of influenza A NP regulates viral genome packaging via interactions with viral RNA and host PI(4,5)P2. *Virology* **496**, 116-126, doi:10.1016/j.virol.2016.05.018 (2016).

63  Alberti, S. Phase separation in biology. *Curr Biol* **27**, R1097-R1102, doi:10.1016/j.cub.2017.08.069 (2017).

64  Elton, D., Medcalf, E., Bishop, K. & Digard, P. Oligomerization of the influenza virus nucleoprotein: identification of positive and negative sequence elements. *Virology* **260**, 190-200, doi:10.1006/viro.1999.9818 (1999).

65  Ramos-Nascimento, A. *et al.* KIF13A mediates trafficking of influenza A virus ribonucleoproteins. *J Cell Sci* **130**, 4038-4050, doi:10.1242/jcs.210807 (2017).

66  Nturibi, E., Bhagwat, A. R., Coburn, S., Myerburg, M. M. & Lakdawala, S. S. Intracellular Colocalization of Influenza Viral RNA and Rab11A Is Dependent upon Microtubule Filaments. *J Virol* **91**, doi:10.1128/JVI.01179-17 (2017).

67  Boeynaems, S. *et al.* Phase Separation of C9orf72 Dipeptide Repeats Perturbs Stress Granule Dynamics. *Mol Cell* **65**, 1044-1055 e1045, doi:10.1016/j.molcel.2017.02.013 (2017).

68  Banerjee, P. R., Milin, A. N., Moosa, M. M., Onuchic, P. L. & Deniz, A. A. Reentrant Phase Transition Drives Dynamic Substructure Formation in Ribonucleoprotein Droplets. *Angew Chem Int Ed Engl* **56**, 11354-11359, doi:10.1002/anie.201703191 (2017).

69  Maharana, S. *et al.* RNA buffers the phase separation behavior of prion-like RNA binding proteins. *Science* **360**, 918-921, doi:10.1126/science.aar7366 (2018).

70  Su, X. *et al.* Phase separation of signaling molecules promotes T cell receptor signal transduction. *Science* **352**, 595-599, doi:10.1126/science.aad9964 (2016).

71  Delarue, M. *et al.* mTORC1 Controls Phase Separation and the Biophysical Properties of the Cytoplasm by Tuning Crowding. *Cell* **174**, 338-349 e320, doi:10.1016/j.cell.2018.05.042 (2018).

72  Sedzicki, J. *et al.* 3D correlative electron microscopy reveals continuity of Brucella-containing vacuoles with the endoplasmic reticulum. *J Cell Sci* **131**, doi:10.1242/jcs.210799 (2018).

73  Phair, R. D., Gorski, S. A. & Misteli, T. Measurement of dynamic protein binding to chromatin in vivo, using photobleaching microscopy. *Methods Enzymol* **375**, 393-414 (2004).